Computational Screening of Single Atoms Anchored on Defective Mo$_2$CO$_2$ MXene Nanosheet as Efficient Electrocatalysts for the Synthesis of Ammonia

Shuo Wang, Lei Li,* Kwan San Hui,* Feng Bin, Wei Zhou, Xi Fan, E. Zalnezhad, Jing Li,* and Kwun Nam Hui*

The electrochemical nitrogen reduction reaction (NRR) over single-atom catalysts (SACs) anchored on Mo vacancies of Mo$_2$CO$_2$ MXene nanosheets under ambient conditions suffers from poor selectivity, low yield, and low Faradaic efficiency because of their sluggish kinetics and the competing hydrogen evolution reaction. Herein, density functional theory calculations are performed to improve the understanding of the selectivity and yielding of ammonia through NRR over various isolated SACs, that is, from Sc to Au, anchored on the Mo vacancy of the Mo$_2$CO$_2$ MXene nanosheet (denoted as MO$_2$CO$_2$-M$_{SA}$). The potential-determining step of the NRR shows that eight candidates (i.e., Y, Zr, Nb, Hf, Ta, W, Re, and Os) confined on the defective Mo$_2$CO$_2$ layer could promote the electroreduction from N$_2$ to NH$_3$. Among these, Mo$_2$CO$_2$-Y$_{SA}$ presented the lowest reported reaction Presents the lowest reported reaction energy barrier (0.08 eV) through the distal pathway and high selectivity to NRR compared with the previously synthesized Mo$_2$CO$_2$-Ru$_{SA}$ with a relatively high energy barrier (0.65 eV) and poor selectivity. In addition, the formation energy of Mo$_2$CO$_2$-Y$_{SA}$ is more negative than that of the Mo$_2$CO$_2$-Ru$_{SA}$ catalyst, suggesting that the experimental preparation of the Mo$_2$CO$_2$-Y$_{SA}$ catalyst is highly feasible. This work lays a solid foundation for improving the rational design of MXene-based systems as efficient electrocatalysts for the synthesis of ammonia.

1. Introduction

The reduction of nitrogen to ammonia (NH$_3$) plays a crucial role in modern society due to its widespread application in agriculture and industrial production.[1] The Haber–Bosch (H–B) process is mainly used in the industrial synthesis of NH$_3$ under high temperature and pressure. Such a process is accompanied by a large consumption of fossil fuels and high CO$_2$ emission.[2] Thus, finding alternative efficient approaches to replace the NH$_3$ production by H–B is of paramount importance for energy conservation and sustainable development.[3] The electrochemical nitrogen reduction reaction (NRR) is an attractive route to produce NH$_3$ due to environment friendliness under ambient conditions.[4] Metal-based materials, single-atom catalysts (SACs), metal-free materials,[5] and their compounds have been explored for the NRR.[6] However, the low activity (large NRR energy barrier), poor selectivity, and low Faraday efficiency

S. Wang, J. Li, K. N. Hui
Joint Key Laboratory of the Ministry of Education, Institute of Applied Physics and Materials Engineering
University of Macau
Avenida da Universidade, Taipa, Macau SAR, Macau, P. R. China
E-mail: victor_li_glv@hotmail.com; bizhui@um.edu.mo

L. Li
Hefei National Laboratory for Physical Sciences at the Microscale, Collaborative Innovation Center of Chemistry for Energy Materials
University of Science and Technology of China
Hefei 230026, P. R. China
E-mail: uestclilei@163.com

K. San Hui
School of Engineering, Faculty of Science
University of East Anglia
Norwich NR4 7TJ, UK
E-mail: k.hui@uea.ac.uk

F. Bin
State Key Laboratory of High-Temperature Gas Dynamics
Institute of Mechanics, Chinese Academy of Science
Beijing 100190, P. R. China

W. Zhou
Department of Mechanical & Electrical Engineering
Xiamen University
Xiamen 361005, P. R. China

X. Fan
Chinese Academy of Sciences
Ningbo Institute of Materials Technology, Engineering
Ningbo 315201, P. R. China

E. Zalnezhad
Department of Chemical and Biomedical Engineering
University of Texas At San Antonio
San Antonio, TX, USA

**ADVANCED
SCIENCE NEWS**
www.advancedsciencenews.com

**ADVANCED
ENGINEERING
MATERIALS**
www.aem-journal.com

of the reported catalysts severely limit their practical industrial applications.

MXene, as a promising catalytic system, has been widely investigated not only in the NRR[7–9] but also in other vital electro-catalytic systems, such as the hydrogen evolution reaction (HER),[10] oxygen evolution reaction (OER),[11] oxygen reduction reaction (ORR),[12] and carbon dioxide reduction.[13] Given their designable structure and unique electronic properties, vacancies in MXene nanosheets provide a platform to effectively stabilize the embedded SACs.[14] This process improves the catalytic activity and atomic utilization of the metal atoms.[15] For example, Pt-SACs supported on defective 2D $Ti_{3-x}C_2T_y$ MXene nanosheets with a Ti vacancy have been prepared via simultaneous self-reduction stabilization, offering a green route for utilizing the greenhouse gas CO_2.[16] Pt-SACs anchored on the surface of Mo vacancies in double-transition metal MXene ($Mo_2TiC_2T_x$) nanosheets resulted in significantly enhanced HER catalytic activity.[15] Ru-SACs embedded on Ti_3C_2 nanosheets have led to a relatively high production yield and selectivity of NH_3 (yield: $2.3\,\mu mol\,h^{-1}\,cm^{-2}$, Faradaic efficiency: 13.13%),[17] surpassing those of other reported catalysts. In addition, Ru-SACs anchored on the surface of Mo vacancies of Mo_2CO_2 MXene nanosheets (Mo_2CO_2-Ru_{SA}) showed considerably enhanced NRR catalytic activity.[8] Nonetheless, it still remains critical for the development and discovery of other single-atom-anchored MXene catalysts with higher NRR catalytic activity.

Nevertheless, through a systematic rational design of an MXene with a specific SAC catalytic center, the inserted N≡N bond may be efficiently activated and the reaction barrier may be reduced, improving the adsorption and activation of N_2 and constructing high-performance NRR catalysts. In addition, because Mo plays an essential role in biological nitrogen fixation systems, a series of Mo-containing materials has been studied as promising NRR catalysts.[18] In this work, first-principles simulation was conducted to better understand the NRR electrocatalytic ability of $3d$, $4d$, and $5d$ transition metal atoms (TMs) embedded on Mo_2CO_2 MXene nanosheets with a Mo vacancy (Mo_2CO_2-V_{Mo}). The products are denoted as Mo_2CO_2-TM_{SA}. Eight candidates were first screened from more than 26 systems according to the lower energy barriers of two possible potential-determining steps (PDSs) of NRR. The structure–property–performance relationship was symmetrically investigated to elucidate the reaction kinetics and mechanism of the NRR. Among these candidates, only Mo_2CO_2-Y_{SA} achieved excellent NRR performance with the lowest onset potential of 0.08 V and high selectivity.

2. Computational Details

Spin-polarized density functional theory (DFT)[19] was conducted for all calculations using the Vienna ab initio Simulation Package (VASP).[20] The projector augmented wave pseudopotential[21] was used to treat the core electrons with a plane-wave cutoff energy of 450 eV, and the Perdew–Burke–Ernzerhof (PBE)[22] exchange-correlation function of the generalized gradient approximation (GGA)[23] was used to describe the electron exchange-correlation interactions. The Mo_2CO_2 supercell was set to $3 \times 3 \times 1$ with a vacuum distance of 20 Å along the

z-direction. The van der Waals interactions were considered using the DFT—D3 correction in Grimme's scheme.[24] The reciprocal space was sampled by $3 \times 3 \times 1$ and $5 \times 5 \times 1$ for geometry optimization and electronic structure calculations, respectively. The maximal convergence tolerance for the force was lower than $0.02\,eV\,Å^{-1}$.[25] The projected crystal orbital Hamilton population (pCOHP) was used to reveal the nature of the bond between the SACs and N-containing intermediates.[26] The thermodynamic stability of catalysts was evaluated by ab initio molecular dynamics (AIMD) simulations for 5 ps at 300 K with a canonical NVT ensemble, in which the number of atoms (N), volume (V), and temperature (T) were set as constant.

3. Free-Energy Calculations

The free-energy diagram of each NRR elementary step was calculated using the computational hydrogen electrode model proposed by Nørskov et al.[27] The free energy of the electron–proton pair ($H^+ + e^-$) can be defined as half of the chemical potential of gaseous H_2 at equilibrium (0 V versus standard hydrogen electrode). The difference of Gibbs free energy can be written as follows

$$\Delta G = \Delta E + \Delta E_{ZPE} - T\Delta S \tag{1}$$

where ΔE is the difference of the reaction energies obtained by DFT calculations, ΔE_{ZPE} is the change in the zero-point energy (ZPE), T is the room temperature ($T = 298.15$ K), and ΔS is the change in entropy calculated by the vibrational frequency analysis. The entropies of the gas molecules (i.e., H_2, N_2, and NH_3) were taken from the NIST database.[28] The detailed calculated energies (E), zero-point energy (E_{ZPE}), and TS for small gas molecules (H_2, N_2, and NH_3) are summarized in Table S2, Supporting Information.

4. Results and Discussion

4.1. Screening Mo_2CO_2-TM_{SA} as eNRR Catalysts

The structure of Mo_2CO_2-TM_{SA} is shown in **Figure 1**a. Defective Mo_2CO_2 had previously been proven to be a suitable platform to stabilize transition metal Ru atoms for electrochemical NRR.[8] Inspired by the experimental findings, we designed and analyzed the NRR performance of a series of single TMs anchored on defective Mo_2CO_2. We removed one surface oxygen atom and replaced the exposed Mo by other transition metals. As shown in Figure 1b, we considered 26 kinds of transition metal elements of $3d$, $4d$, and $5d$ period with a black tag because of the feasibility of their preparation.[15] To systematically explore and screen the NRR performance of Mo_2CO_2-TM_{SA}, we proposed four criteria based on the previous literature,[29,30] namely, N_2 adsorption, the first N_2 hydrogenation, the last NH_3 formation, and the formation energies of Mo_2CO_2-TM_{SA}.

According to the aforementioned criteria, we first calculated the configuration of the N_2 adsorption on each Mo_2CO_2-TM_{SA}. Given that the physical or chemical N_2 adsorption on the active sites is the first step of the NRR, we tested both end-on and
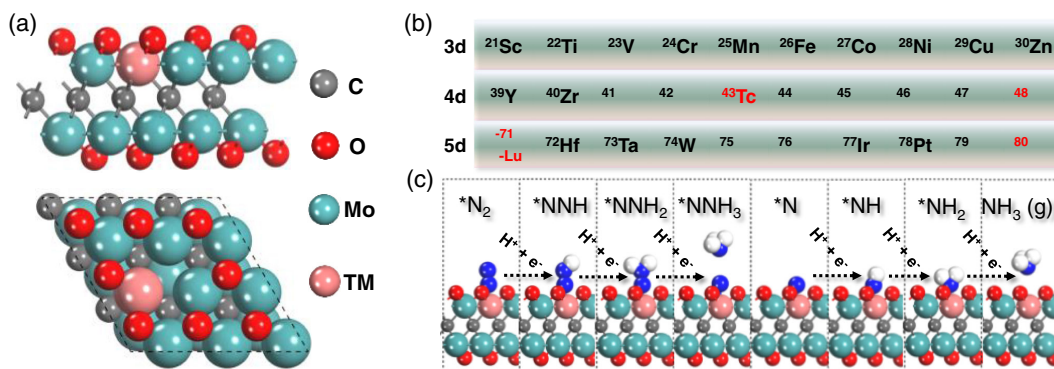
Figure 1. Atomic models and the distal pathway of nitrogen reduction. a) Top and side views of the single-transition metal atom catalyst anchored on the Mo_2CO_2-TM_{SA} matrix. b) A total of 26 kinds of transition metals with black tag are considered. c) Scheme of proton-coupled electron transfer for nitrogen reduction via a distal pathway.

side-on adsorption configurations by geometry optimization. Despite the creation of a three-metal interspace as active site by the oxygen vacancy, N_2 is still difficult to adsorb on the Mo_2CO_2 surface by side-on mode. This phenomenon is due to the two negative charges repelled by the covered oxygen elements and steric effect. Hence, the initial adsorption configurations should be more favorable to end-on mode on the single-atom site. Our calculation results further confirmed that the thermodynamically favorable interaction structure of N_2 after structural optimization indicated that all side-on configurations were transformed to end-on configurations. The distance between the metal site and the adjacent N atom ranged from 2.041 Å (for Mo) to 2.991 Å (for Os), and the adsorption energy of N_2 on the transition metal site was also calculated to be in the range from -0.10 eV (for Ru) to -0.59 eV (for Mo). This result indicated that N_2 was mainly adsorbed on Mo_2CO_2-TM_{SA} by physical adsorption. The N—N bond length was also slightly elongated after adsorption compared with that of pristine N_2. The detailed results of the bond length and adsorption energy are listed in Table S1, Supporting Information. Combined with the results from N_2 adsorption and previous studies based on the MXene substrate,[29] N_2 should be activated via a distal reaction pathway as shown in Figure 1c. Starting from the *N_2-adsorbed state, the N atom far from the catalytic center was attacked by three consecutive proton–electron pairs ($H^+ + e^-$) until the first NH_3 molecule was formed and released. Consequently, the remaining N atom was attacked by another three proton–electron pairs ($H^+ + e^-$). Finally, the last NH_3 molecule was released. The detailed process of the total six-electron NRR is provided in our Supporting Information (Equation (S1)–(S10), Supporting Information).

Previous studies have demonstrated that the first N_2 hydrogenation (*N_2→*NNH) and the last NH_3 formation (*NH_2→*NH_3) were usually described as the potential-determining steps of the whole N_2 reduction process. With respect to the limited potential-determining step of each of the six different proton–electron elementary steps for the NRR, the difference in the Gibbs energies of the N_2 hydrogenation and NH_3 formation should be minimized. Therefore, we calculated these two vital parameters on Mo_2CO_2-TM_{SA} to rapidly screen the NRR candidates. The results of $\Delta G_{(*N2\rightarrow*NNH)}$ versus
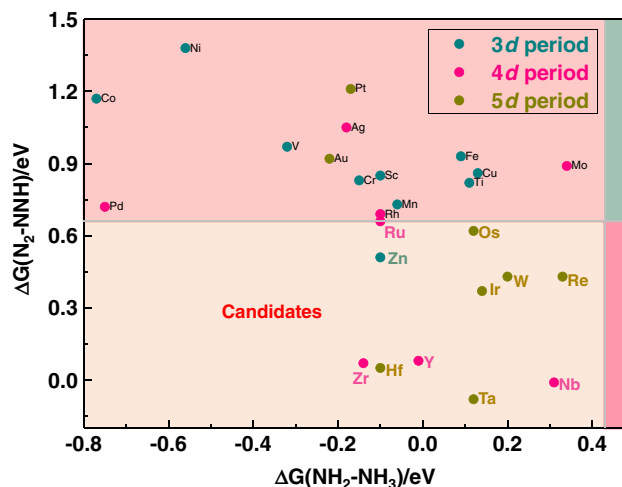
Figure 2. Screening results of Mo_2CO_2-M_{SA} for NRR based on the changes in the free energy of the first and last hydrogenation steps, namely, ΔG (N_2—NNH) and ΔG (NH_2—NH_3), respectively. The materials corresponding to the points in the lower-left area are candidates for further investigation on the NRR processes.

$\Delta G_{(*NH2\rightarrow*NH3)}$ for the investigated Mo_2CO_2-TM_{SA} are plotted in **Figure 2**. Ru anchored on a defective Mo_2CO_2 matrix was successfully synthesized experimentally, and their good NRR performance was further proved.[8] Thus, the difference in the Gibbs energy of Mo_2CO_2-Ru_{SA} could be used as a benchmark for screening possible NRR materials. According to the first-principles calculation, $\Delta G_{(*N2\rightarrow*NNH)}$ and $\Delta G_{(*NH2\rightarrow*NH3)}$ of Mo_2CO_2-Ru_{SA} were calculated to be as high as 0.65 and -0.11 eV, respectively. Considering both calculations' results and some typical theoretical literature,[30,31] we finally selected 0.65 and 0.43 eV as the activity criteria for $\Delta G_{(*N2\rightarrow*NNH)}$ and $\Delta G_{(*NH2\rightarrow*NH3)}$ for the different Mo_2CO_2-TM_{SA}, respectively. The potential-determining energy of possible NRR catalysts should be close to or smaller than our defined criteria. Therefore, only the Mo_2CO_2-TM_{SA} in the lower left region, including the defective Mo_2CO_2 anchored with 3d period (Zn), 4d period (Y, Zr, and Nb), and 5d period (Hf, Ta, W, Re, Os,

and Ir), were considered for the following studies. Most of the $3d$ metal catalytic sites, except Zn, show poor N_2 hydrogenation performance. However, numerous $4d$ and $5d$ metal sites, especially at the first half period, showed a good N_2 hydrogenation performance. The ionic radius and electrons were related to the NRR performance in our systems, which will be analyzed *vide infra*.

Here, we further investigated the synthetic accessibility and the thermal stability of the screened candidates by computing their formation energies (E_f) and AIMD. Generally, a material with more negative value of E_f can be synthesized in the laboratory. In contrast, materials with positive values of E_f are difficult to synthesize. Given that Mo_2CO_2-Ru_{SA} was successfully synthesized in the experiments, the formation energy of our potential active materials should be lower than that of Mo_2CO_2-Ru_{SA}. For Zn, Y, Zr, Nb, Hf, Ta, W, Re, Os, and Ir embedded in the defective Mo_2CO_2, the formation energies were $+5.48$, -1.74, -3.97, -3.63, -4.03, -4.20, -2.90, -0.52, -0.91, and $+0.77$ eV, respectively. Compared with the E_f criterion of Mo_2CO_2-Ru_{SA} (-0.35 eV), Mo_2CO_2-Zn_{SA} and Mo_2CO_2-Ir_{SA} should be ruled out in the candidates. Moreover, AIMD simulations were further performed to evaluate the thermodynamic stability of the remaining eight candidates, which were tested at 300 K for 5 ps with a

time step of 1 fs. As shown in Figure S1–S8, Supporting Information, the energy and temperature of all the candidates oscillated within a narrow range, and the geometric structure was basically unchanged. The results indicated that the structures of Y, Zr, Nb, Hf, Ta, W, Re, and Os anchored on the defective Mo_2CO_2 can remain stable at 300 K. Therefore, all the candidates could be synthesized and serve as NRR electrocatalysts at ambient conditions with high stability. Finally, nearly one-third of the candidates (8/26) were screened to evaluate the whole NRR process.

4.2. Reaction Mechanism and NRR Activity of Candidates

The complete reaction mechanism was investigated to evaluate the potential of the eight candidates to determine the specific hydrogenation reaction steps of the NRR catalysts. According to our earlier analysis and some previous studies based on defective MXene systems, an end-on N_2 adsorption model along with a distal pathway was more favorable than the alternating pathway because of the special coordinated environment of the substrate of the former. The free-energy diagrams of the eight candidates are plotted in **Figure 3**a–i to elucidate the NRR mechanism in
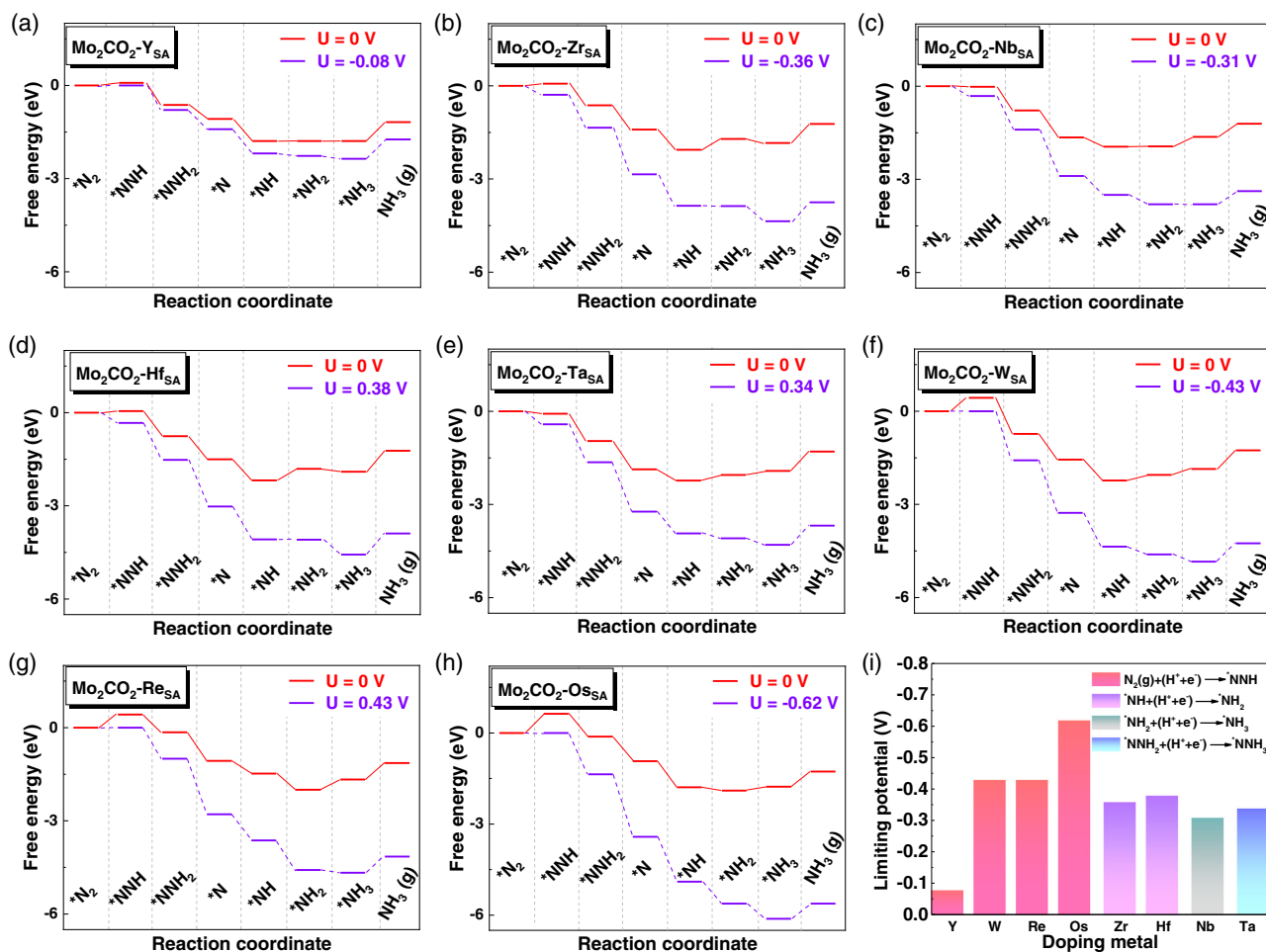
Figure 3. a–h) Free-energy diagrams for the whole NRR process of the eight candidates at different potentials. i) Summary of limiting potentials for eNRR via a distal pathway for transition metal single-atom catalysts on Mo_2CO_2-V_{Mo}.

detail. In addition, the corresponding configurations for each elementary step are shown in Figure S9–S16, Supporting Information. To compare the theoretical simulation and experiments, the pristine Mo_2CO_2 with only one oxygen vacancy (denoted as Mo_2CO_2-Mo_{SA}) and experimentally synthesized defective Mo_2CO_2-Ru_{SA} were also considered here, and their free-energy profiles are shown in Figure S17 and S18, Supporting Information, respectively. For metal catalysts, the Ru(0001) surface was considered to have the highest activity and was selected as a benchmark for comparison.[32]

The theoretical limiting potential (U_L) is often used to evaluate the intrinsic activity of catalysts. This potential is the lowest negative potential, i.e., $U_L = -\Delta G_{max}/e$, where ΔG_{max} is the maximum change in the free energy of the proton–electron step. The summarized potential-determining step and related energies of the selected candidates, Mo_2CO_2-Mo_{SA} and Mo_2CO_2-Ru_{SA}, are shown in **Table 1**. The limiting potential of the eight candidates surpassed that of the metal-based benchmark Ru(0001) ($U_L = -1.08$ V). On the basis of Y (-0.08 V), Zr (-0.36 V), and Nb (-0.31 V) for the $4d$ metals and Hf (-0.38 V), Ta (-0.34 V), W (-0.43 V), Re (-0.43 V), and Os (-0.62 V) for the $5d$ metals, eight candidates (i.e., Mo_2CO_2-Y_{SA}, Mo_2CO_2-Zr_{SA}, Mo_2CO_2-Nb_{SA}, Mo_2CO_2-Hf_{SA}, Mo_2CO_2-Ta_{SA}, Mo_2CO_2-W_{SA}, Mo_2CO_2-Re_{SA}, and Mo_2CO_2-Os_{SA}) also exhibited significantly lower limiting potential compared with Mo_2CO_2-Mo_{SA} (-0.89 eV) and experimentally prepared Mo_2CO_2-Ru_{SA} (-0.65 eV). Among the candidates, the PDS of the Y, W, Re, Nb, and Os system perfectly matched our defined screening criteria, which depended on the first N_2 hydrogenation ($*N_2 \rightarrow *NNH$) or the last NH_3 formation ($*NH_2 \rightarrow *NH_3$). However, the PDSs of the other three candidates were not the same as our criteria, as shown in Figure 3i. The PDSs of the Zr and Hf system were from $*NNH$ to $*NNH_2$, whereas that of the Ta system was from $*NNH_2$ to $*NNH_3$. Despite the differences, our screening criteria were still efficient to filter out some catalysts with higher limiting potentials. The limiting potentials of all selected candidates were not higher than our initial set value of 0.65 eV. Moreover, the potential-determining steps of $*NNH$ to $*NNH_2$ and $*NNH_2$ to $*NNH_3$ have also been proved to be essential steps of the NRR process, according to previous studies.[29,30]

Table 1. Detailed information of eight candidates, Mo_2CO_2-Mo_{SA}, and Mo_2CO_2-Ru_{SA} for comparison. Elements are arranged by atomic number. Mo_2CO_2-Y_{SA} with the lowest ΔG_{max} highlighted.

	$\Delta E_{N2\text{-adsorption}}$ (eV)	PDS	ΔG_{max} (eV)	$\Delta G_{NH3\text{-desorption}}$ (eV)
Y	-0.31	$*N_2 \rightarrow *NNH$	0.08	0.61
Zr	-0.26	$*NH \rightarrow *NH_2$	0.36	0.61
Nb	-0.28	$*NH_2 \rightarrow *NH_3$	0.31	0.42
Mo	-0.59	$*N_2 \rightarrow *NNH$	0.89	0.41
Ru	-0.07	$*N_2 \rightarrow *NNH$	0.65	0.35
Hf	-0.26	$*NH \rightarrow *NH_2$	0.38	0.67
Ta	-0.19	$*NNH_2 \rightarrow *NNH_3$	0.34	0.62
W	-0.23	$*N_2 \rightarrow *NNH$	0.43	0.59
Re	-0.35	$*N_2 \rightarrow *NNH$	0.43	0.52
Os	-0.22	$*N_2 \rightarrow *NNH$	0.62	0.50

The final NH_3 desorption process would significantly affect the yield of gas release. Previous studies have indicated that $\Delta G_{NH3\text{-desorption}}$ in the NRR was in the range 0.4–1.3 eV.[33] This value implied that the high energy of $G_{NH3\text{-desorption}}$ would inhibit the final NH_3 release. In our case, the NH_3 desorption processes of all candidates were endothermic in the narrow range (from 0.42 to 0.67 eV), and most values were lower than those of the majority of the reported SAC-supported MXene-based NRR catalysts, such as $W/Ti_{2-x}C_2O_y$ (0.95 eV),[34] $Mo_2TiC_2O_2$-Zr_{SA} (0.97 eV),[29] and Mn/Nb_2CN_2 (0.58 eV).[33] Thus, all candidates should be recycled experimentally and have high efficiency. Then, we analyzed the Bader charge of a series of TMs to gain insight into the screening results, as displayed in Figure S19, Supporting Information. The positive charge of the $3d$ TMs were all below $2.00|e|$, whereas the partial charge on the dopants of $4d$ and $5d$ generally decreased because the number of valence electrons increased. More importantly, the dopants, including Y, Zr, Nb, Hf, Ta, W, and Re, showed better screening results in the first half-period when the positive charge was $\approx 2.00|e|$. A positively charged center can obviously polarize and activate the inert N_2 molecule.[35] Hence, doping of these SACs with larger positive charges could significantly promote the NRR process. Furthermore, the main side reaction competing with the NRR in an acidic environment was the HER. The limiting potential (U_L) of the HER is the applied potential; that is, the step on the considered process was the most exergonic. The differences in the free energies of hydrogen adsorption were calculated on the same site of the NRR activities. The relationship[36] between $U_{L(HER)}$ and $U_{L(NRR)}$ for the eight candidate systems are shown in Figure S20, Supporting Information, and the related HER diagrams are shown in Figure S21, Supporting Information. All candidates should have remarkably higher NRR performance than the HER. Thus, all candidates are ideal electrocatalysts for the NRR because of their moderate positive charge and inhibiting effect on the HER.

Considering that Mo_2CO_2-Y_{SA} exhibited the lowest theoretical limiting potential among the candidates, we took Mo_2CO_2-Y_{SA} as an example to examine the whole free-energy diagram in Figure 3a and Figure S22, Supporting Information. At the beginning, N_2 was intensely physisorbed on the single Y atom in an end-on configuration with the N—N bond length of 1.12 Å, and the distance between Y and the adjacent nitrogen was 2.61 Å. Then, the first proton coupled with an electron ($H^+ + e^-$) attacked the adsorbed $*N_2$ to produce the $*NNH$ intermediate, with the N—N bond extended to 1.27 Å. This step activated the high stability of the triple bond of the N_2 molecule and resulted in the maximum differences in the free energies of 0.08 eV. The subsequent changes in the free energy after the first step were almost downhill until the final NH_3 was released with a relatively low energy of 0.61 eV. The detailed calculated energies (E), zero-point energy (E_{ZPE}), and TS for N-containing Intermediates ($*N_2$, $*NNH$, $*NNH_2$, $*NNH_3$, etc.) are summarized in Table S3, Supporting Information. The unique advantages of the single-atom Y anchored on the defective MoC_2O_2 were its extremely low limiting potential (-0.08 V) and moderate NH_3 desorption ability (0.61 eV), which were better than those of the majority of the reported single-atom-doped MXenes, including $W/Ti_{2-x}C_2O_y$ (-0.11 V and 0.95 eV),[34] $Ru@Mo_2CO_2$ (-0.46 V and 0.59 eV),[37] $Mo_2TiC_2O_2$-Zr_{SA} (-0.15 V and 0.97 eV),[29]

and Mn-Nb$_2$C2$-$0.51 V and 0.58 eV).[33] These characteristics indicated that Mo$_2$CO$_2$-Y$_{SA}$ would require lower applied potential to initiate the reaction toward producing ammonia at an appropriate rate and, therefore, have better intrinsic activity.

4.3. Origin of NRR Activity on Mo$_2$CO$_2$-M$_{SAC}$

Based on the free-energy diagrams, further clarification of the meaningful activity trends is very essential to provide a panorama of Mo$_2$CO$_2$-TM$_{SA}$ for the NRR. Electronic combinations of filled and empty d orbitals for the transition metals are well known to determine the reduction performance.[38,39] As shown in **Figure 4**, TM atoms have empty d orbitals that accept lone-pair electrons from the N$_2$ molecule to form an σ bond, and they can also feed electrons back to the antibonding orbital of the N$_2$ molecule to form a π* bond and then weaken the inert N≡N triple bond.[38] Therefore, the charge density differences were performed to visually prove the electronic transfer between the active site and N$_2$, as described in Figure S23 and S24, Supporting Information. All active sites could effectively activate N$_2$. The charge accumulation (yellow region) was distributed around the N≡N and N─M$_{SA}$ bonds, whereas charge depletion (cyan region) around the N≡N bonds and N─M$_{SA}$ bonds was clearly observed. These results implied that N$_2$ could be activated when interacting with these TM atoms.

Previous sections have shown that the variation in the charge at each active site determined whether the N≡N triple bond could be activated and indirectly affected the limiting potential. However, the underlying origin between the different metal centers of Mo$_2$CO$_2$-M$_{SA}$ and ΔE_{*N2} trends remain to be explained. To reveal the underlying mechanism and the role of the different metal centers, we analyzed the various electronic structures of the screened Mo$_2$CO$_2$-TM$_{SA}$.

As shown in Figure S25, Supporting Information, the variation in local density of state (LDOS) was plotted near the Fermi level for the adsorbed N$_2$ on Mo$_2$CO$_2$-TM$_{SA}$ compared with the free N$_2$ molecule. The molecular orbitals of the free N$_2$ molecule mainly consisted of 2σ, 2σ*, 1π, 3σ, and 1π* around the Fermi level (as shown in Figure S25i, Supporting Information). This result was similar to previous theoretical results.[7,40] After N$_2$ was adsorbed on the different single atoms, the peak intensity of each orbital of N$_2$ was weakened, and the peak shape of the orbital changed from the original slender and sharp peak to a wide and rounded one. The 1π orbital nearly disappeared, indicating that the N≡N triple bond was effectively weakened. The 1π* orbital downshifted toward the Fermi level, reflecting the accepted electrons from the M-d orbitals, especially

for doping Y, in which the 1π* orbital downshifted at ≈1.5 eV, which is closer to the Fermi level than other cases. The electron accepting–donating interaction was directly reflected by the overlap between the N$_2$ orbitals and M-d orbital as shown in the LDOS. This result was consistent with the peak of N$_2$-1π* shifting away from Fermi level as the TM atomic number became larger in the same period. The increased overlapping, that is, as the TM element changed from left to right in the same period, corresponded to the decreased electron interaction between the M-d and N$_2$ and the weakened N≡N triple bond.

We further introduced the pCOHP to analyze the interaction between the metal active center and the nitrogen adatom. We followed the usual method to display COHPs; that is, bonding states were drawn to the right, and antibonding states were drawn to the left, which represented the negative and positive contributions, respectively. For Mo$_2$CO$_2$-Y$_{SA}$ (**Figure 5**a), bonding orbital populations were detected mainly in the valence bands (below E_F), and a small part appeared in the conduction band. Meanwhile, the antibonding states were mainly distributed in the conduction band. These phenomena explained the strong adsorption of *N$_2$ on Mo$_2$CO$_2$-Y$_{SA}$. However, for the doping elements Zr, Nb, Hf, Ta, W, Re, and Os, as shown in Figure 5b–i, the increase in the fillings of both bonding and antibonding orbital populations with the antibonding orbitals was below E_f, which is in accordance with the decreasing binding strength as indicated by the more positive ΔE_{*N2}. In addition, we calculated the integrated COHP (ICOHP) by calculating the energy integral at the E_f, which directly exhibited a slightly quantitative demonstration between ICOHP and ΔE_{*N2}, as shown in Figure S26, Supporting Information. This trend indicated that the filling of the antibond orbitals below the Fermi level tended to be weak N$_2$ adsorption. This result validated the effect of various metal centers in determining the bonding/antibonding orbital populations on the NRR activity trends.

5. Conclusion

In summary, we systematically investigated the potential of various TM-SACs anchored on the Mo vacancy of Mo$_2$CO$_2$ nanosheets on the basis of first-principles computations. By considering the first and last hydrogenation steps as the criteria, we screened eight candidates, including Y, Zr, Nb, Hf, Ta, W, Re, and Os, anchored on the defective Mo$_2$CO$_2$. All candidates could be synthesized in the laboratory due to their lower formation energy and stable dynamic performance compared with those of Mo$_2$CO$_2$-Ru$_{SA}$. Mo$_2$CO$_2$-Y$_{SA}$ has been reported as a
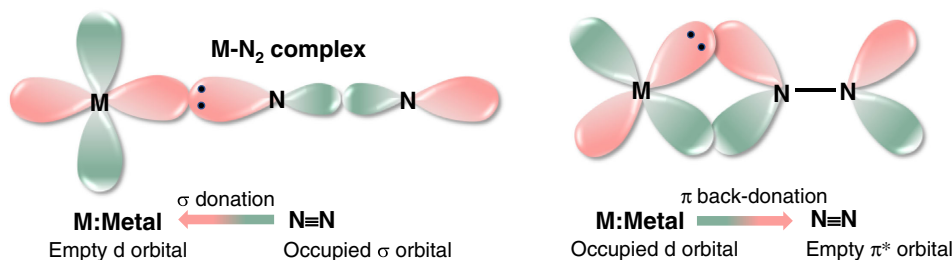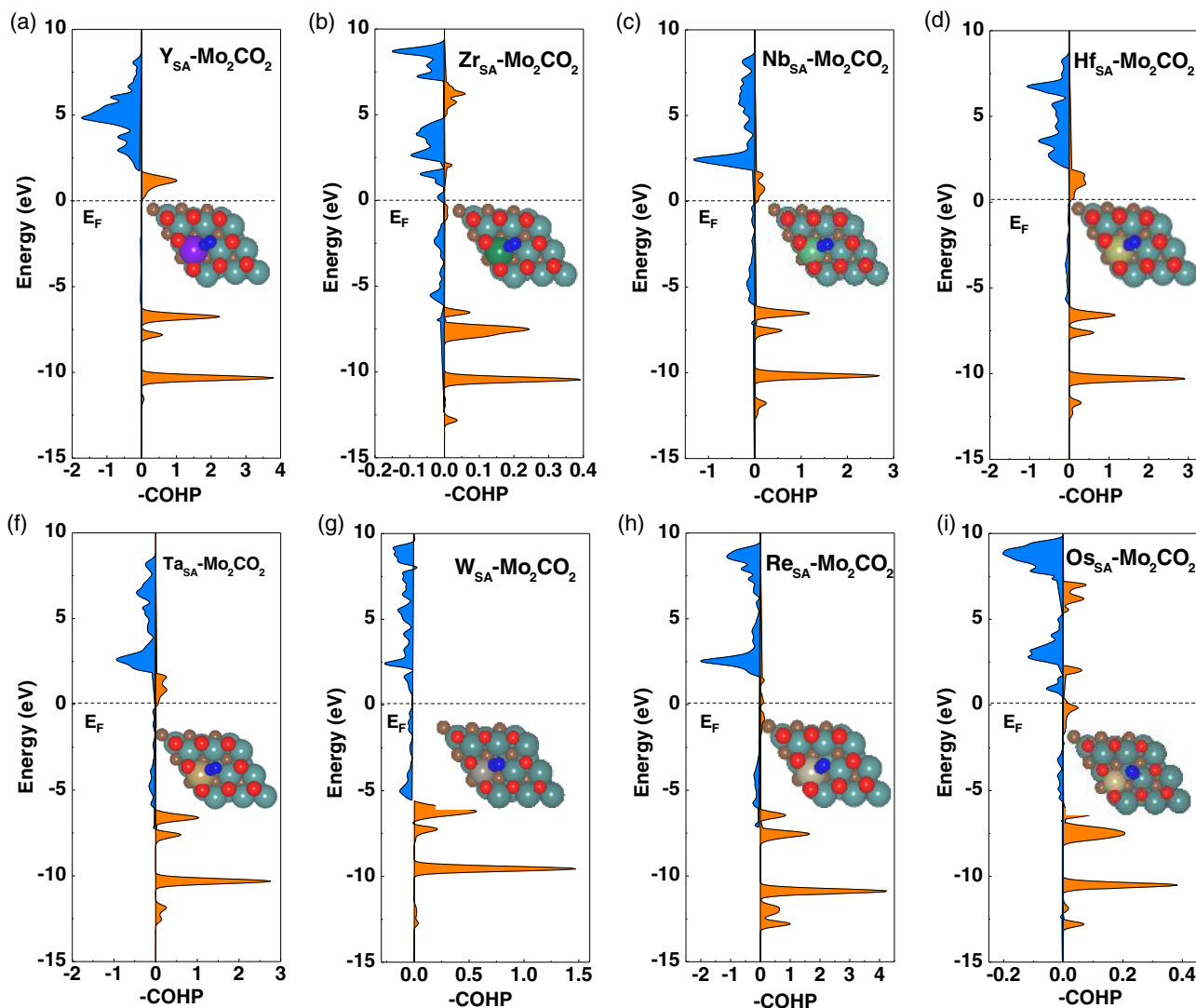

Figure 4. Simplified schematics of N2 bonding to a transition metal atom.

Figure 5. a–i) Projected crystal orbital Hamilton population (pCOHP) between the metal center and the nitrogen adatom. Orange stands for bonding contributions and blue stands for antibonding contributions.

promising candidate for the NRR with a low limiting potential of −0.08 V and excellent selectivity. This work not only provided a novel type of TM-SAC supported on defective MXenes for the synthesis of ammonia, but also proposed a systematic strategy for screening NRR electrocatalysts, which can be extended to other materials.

Supporting Information

Supporting Information is available from the Wiley Online Library or from the author.

Conflict of Interest

The authors declare no conflict of interest.

Data Availability Statement

Data sharing is not applicable to this article as no new data were created or analyzed in this study.

[1] a) X. Chen, N. Li, Z. Kong, W.-J. Ong, X. Zhao, *Mater. Horiz.* **2018**, *5*, 9; b) I. Coric, B. Q. Mercado, E. Bill, D. J. Vinyard, P. L. Holland, *Nature* **2015**, *526*, 96.

[2] X. Yang, J. Nash, J. Anibal, M. Dunwell, S. Kattel, E. Stavitski, K. Attenkofer, J. G. Chen, Y. Yan, B. Xu, *J. Am. Chem. Soc.* **2018**, *140*, 13387.

[3] A. Klerke, C. H. Christensen, J. K. Nørskov, T. Vegge, *J. Mater. Chem.* **2008**, *18*, 2304.

[4] J. H. Montoya, C. Tsai, A. Vojvodic, J. K. Nørskov, *Chemsuschem* **2015**, *8*, 2180.

[5] Y. Li, D. Gao, S. Zhao, Y. Xiao, Z. Guo, Y. Fang, J. Lin, Z. Liu, Y. Huang, K. Guo, C. Tang, *Chem. Eng. J.* **2021**, *410*, 128419.

[6] a) B. Yang, W. Ding, H. Zhang, S. Zhang, *Energy Environ. Sci.* **2021**, *14*, 672; b) H. Niu, X. Wang, C. Shao, Z. Zhang, Y. Guo, *ACS Sustainable Chem. Eng.* **2020**, *8*, 13749.

[7] S. Wang, B. Li, L. Li, Z. Tian, Q. Zhang, L. Chen, X. C. Zeng, *Nanoscale* **2020**, *12*, 538.

[8] W. Peng, M. Luo, X. Xu, K. Jiang, M. Peng, D. Chen, T. S. Chan, Y. Tan, *Adv. Energy Mater.* **2020**, *10*, 2070110.

[9] a) X. Guo, J. Gu, S. Lin, S. Zhang, Z. Chen, S. Huang, *J. Amer. Chem. Soc.* **2020**, *142*, 5709; b) X. Xu, B. Sun, Z. Liang, H. Cui, J. Tian, *ACS Appl. Mater. Interfaces* **2020**, *12*, 26060; c) J. Sun, W. Kong, Z. Jin, Y. Han, L. Ma, X. Ding, Y. Niu, Y. Xu, *Chin. Chem. Lett.* **2020**, *31*, 953; d) Y. Luo, G.-F. Chen, L. Ding, X. Chen, L.-X. Ding, H. Wang, *Joule* **2019**, *3*, 279.

[10] X. Wang, C. Wang, S. Ci, Y. Ma, T. Liu, L. Gao, P. Qian, C. Ji, Y. Su, *J. Mater. Chem. A* **2020**, *8*, 23488.

[11] T. Y. Ma, J. L. Cao, M. Jaroniec, S. Z. Qiao, *Angew. Chem. Int. Ed.* **2016**, *55*, 1138.

[12] a) C.-Y. Liu, E. Y. Li, *ACS Appl. Mater. Interfaces* **2019**, *11*, 1638; b) H. Lin, L. Chen, X. Lu, H. Yao, Y. Chen, J. Shi, *Sci. China Mater.* **2019**, *62*, 662.

[13] a) Y. Yan, J. Chen, N. Li, J. Tian, K. Li, J. Jiang, J. Liu, Q. Tian, P. Chen, *ACS Nano* **2018**, *12*, 3523; b) Y. Xiao, W. Zhang, *Nanoscale* **2020**, *12*, 7660; c) L. Li, B. Li, H. Guo, Y. Li, C. Sun, Z. Tian, L. Chen, *Nanoscale* **2020**, *12*, 15880.

[14] A. Liu, X. Liang, X. Ren, W. Guan, M. Gao, Y. Yang, Q. Yang, L. Gao, Y. Li, T. Ma, **2020**, *30*, 2003437.

[15] J. Zhang, Y. Zhao, X. Guo, C. Chen, C.-L. Dong, R.-S. Liu, C.-P. Han, Y. Li, Y. Gogotsi, G. Wang, *Nat. Catal.* **2018**, *1*, 985.

[16] X. Zhang, J. Lei, D. Wu, X. Zhao, Y. Jing, Z. Zhou, *J. Mater. Chem. A* **2016**, *4*, 4871.

[17] A. Liu, M. Gao, X. Ren, F. Meng, Y. Yang, Q. Yang, W. Guan, L. Gao, X. Liang, T. Ma, *Nanoscale* **2020**, *12*, 10933.

[18] a) B. K. Burgess, D. J. Lowe, *Chem. Rev.* **1996**, *96*, 2983; b) E. E. Stüeken, R. Buick, B. M. Guy, M. C. Koehler, *Nature* **2015**, *520*, 666; c) J. Zhao, Z. Chen, *J. Am. Chem. Soc.* **2017**, *139*, 12480; d) L. Jasin Arachchige, Y. Xu, Z. Dai, X. Zhang, F. Wang, C. Sun, *J. Phys. Chem. C* **2020**, *124*, 15295; e) L. Li, B. Li, Q. Guo, B. Li, *J. Phys. Chem. C* **2019**, *123*, 14501.

[19] S. Grimme, *J. Comput. Chem. Mater.* **2006**, *27*, 1787.

[20] G. Kresse, J. Furthmüller, *Phys. Rev. B* **1996**, *54*, 11169.

[21] P. E. Blöchl, *Phys. Rev. B* **1994**, *50*, 27.

[22] J. P. Perdew, Y. Wang, *Phys. Rev. B Condens. Matter.* **1992**, *46*, 12947.

[23] J. P. Perdew, K. Burke, M. Ernzerhof, *Phys. Rev. Lett.* **1996**, *77*, 3865.

[24] S. Grimme, J. Antony, S. Ehrlich, H. Krieg, *J. Chem. Phys.* **2010**, *132*, 1.

[25] H. J. Monkhorst, J. D. Pack, *Phys. Rev. B* **1976**, *13*, 5188.

[26] S. Maintz, V. L. Deringer, A. L. Tchougréeff, R. Dronskowski, *J. Comput. Chem.* **2016**, *37*, 1030.

[27] a) A. A. Peterson, F. Abild-Pedersen, F. Studt, J. Rossmeisl, J. K. Nørskov, *Energy Environ. Sci.* **2010**, *3*, 1311; b) J. Rossmeisl, A. Logadottir, J. K. Nørskov, *Chem. Phys.* **2005**, *319*, 178.

[28] J. Carper, *Lib. J.* **1999**, *124*, 192.

[29] L. Li, X. Wang, H. Guo, G. Yao, H. Yu, Z. Tian, B. Li, L. Chen, *Small Methods* **2019**, *3*, 1900337.

[30] C. Ling, Y. Ouyang, Q. Li, X. Bai, X. Mao, A. Du, J. Wang, *Small Methods* **2019**, *3*, 1800376.

[31] T. He, A. R. Puente Santiago, A. Du, *J. Catal.* **2020**, *388*, 77.

[32] E. Skúlason, T. Bligaard, S. Gudmundsdóttir, F. Studt, J. Rossmeisl, F. Abild-Pedersen, T. Vegge, H. Jónsson, J. K. Nørskov, *Phys. Chem. Chem. Phys.* **2012**, *14*, 1235.

[33] Y. Kong, D. Liu, H. Ai, K. H. Lo, S. Wang, H. Pan, *ACS Appl. Nano Mater.* **2020**, *3*, 11274.

[34] S. Tang, T. Liu, Q. Dang, X. Zhou, X. Li, T. Yang, Y. Luo, E. Sharman, J. Jiang, *J. Phys. Chem. Lett.* **2020**, *11*, 5051.

[35] C. Choi, S. Back, N.-Y. Kim, J. Lim, Y.-H. Kim, Y. Jung, *ACS Catal.* **2018**, *8*, 7517.

[36] Y. Li, D. Gao, S. Zhao, Y. Xiao, Z. Guo, Y. Fang, J. Lin, Z. Liu, Y. Huang, K. Guo, C. Tang, *Chem. Eng. J.* **2021**, *410*.

[37] B. Huang, N. Li, W.-J. Ong, N. Zhou, *J. Mater. Chem. A* **2019**, *7*, 27620.

[38] M.-A. Légaré, G. Bélanger-Chabot, R. D. Dewhurst, E. Welz, I. Krummenacher, B. Engels, H. Braunschweig, *Science* **2018**, *359*, 896.

[39] C. Ling, X. Niu, Q. Li, A. Du, J. Wang, *J. Am. Chem. Soc.* **2018**, *140*, 14161.

[40] H.-R. Zhu, Y.-L. Hu, S.-H. Wei, D.-Y. Hua, *J. Phys. Chem. C* **2019**, *123*, 4274.